

## Supplemental Information

### UV Activation of Polymeric High Aspect Ratio Microstructures: Ramifications in Antibody Surface Loading For Circulating Tumor Cell Selection

Joshua M. Jackson,<sup>1#</sup> Małgorzata A. Witek,<sup>2#</sup> Mateusz L. Hupert,<sup>2</sup> Charles Brady,<sup>2</sup> Swathi Pullagurla,<sup>3</sup>

Joyce Kamande,<sup>3</sup> Rachel Aufforth,<sup>4</sup> Christopher J. Tignanelli,<sup>5</sup> Robert J. Torphy,<sup>6</sup> Jen Jen Yeh,<sup>4-8</sup> and

Steven A. Soper<sup>1,2,9\*</sup>

<sup>1</sup>Department of Chemistry, UNC-Chapel Hill, NC

<sup>2</sup>Department of Biomedical Engineering, UNC-Chapel Hill, NCSU, Raleigh, NC

<sup>3</sup>Department of Chemistry, Louisiana State University, Baton Rouge, LA

<sup>4</sup>Division of Surgical Oncology, UNC, Chapel Hill, NC

<sup>5</sup>Department of Surgery, UNC, Chapel Hill, NC

<sup>6</sup>School of Medicine, UNC, Chapel Hill, NC

<sup>7</sup>Department of Pharmacology, UNC, Chapel Hill, NC

<sup>8</sup>Lineberger Comprehensive Cancer Center, UNC, Chapel Hill, NC

<sup>9</sup>Ulsan National Institute of Science and Technology, South Korea

# These authors contributed equally

\*corresponding author ssoper@unc.edu

## Experimental Methods

**Immobilization of anti-EpCAM antibodies to polymer surfaces for CTC selection.** Antibody immobilization was carried out in a two-step process. A UV-activated thermally assembled device was loaded with a solution containing 20 mg mL<sup>-1</sup> EDC and 2 mg mL<sup>-1</sup> NHS in 100 mM MES (pH = 4.8) for 15 min at room temperature to obtain a succinimidyl ester intermediate. After this incubation, the EDC/NHS solution was removed by aspirating through the microchip with a vacuum pump followed by immediately flooding the chip with an aliquot of a solution containing 0.5 mg mL<sup>-1</sup> of the monoclonal anti-EpCAM antibody in 150 mM PBS (pH = 7.4). The reaction was allowed to proceed at 4°C overnight. The device was then rinsed (4 mm s<sup>-1</sup>) with 2 mL of PBS/0.5% BSA (pH = 7.4) to remove any non-specifically bound anti-EpCAM antibody.

**Patient Derived Xenografts (PDX) models for pancreatic ductal adenocarcinoma (PDAC).** Nude mice (6-8 weeks of age) were purchased from Harlan Sprague Dawley. The mice were anesthetized with 100 mg kg<sup>-1</sup> ketamine and 1 mg kg<sup>-1</sup> domitor. When the proper plane of anesthesia was reached, a sterile ophthalmic gel was placed in each eye. The injection area was sterilized with ethanol and betadaine. A flank xenograft procedure was as follows: (i) a 3 mm incision was made on each flank by lifting the skin with forceps and cutting with microdissecting scissors; (ii) hemostat forceps were used to loosen the skin inside the incision for subsequent tumor implantation, which was obtained from a patient biopsy sample possessing a tissue biopsy sample from a metastatic pancreatic ductal adenocarcinoma patient; (iii) a maximum of three 1 mm matrigel-coated pancreatic tissue cubes were then transferred into the subcutaneous space of each incision; (iv) the incision was closed with a Nexaband liquid and simple interrupted sutures using monofilament 3-0 nylon (Maxon) or surgical clips; and (v) 500 µL of 0.9% sterile saline was injected IP. The mouse was transferred to a recovery area and was warmed with a heating blanket. Lidocaine was used pre-operatively as an analgesic. After the procedure, the anesthesia was reversed with an injection of anti-sedan. Tumors were grown for 8 weeks, after which whole blood was collected from the IVC into sodium citrate tubes (final concentration, 0.38%).

## Results and Discussion

**UV-visible absorption spectra of polymer substrates.** Sheets (250 µm thick) of PMMA, COC, and PC were UV-activated for 15 min (254 nm, 22 mW/cm<sup>2</sup>). At several time increments, the UV-Vis spectra of these sheets were acquired to observe the polymers' transmittance as a function of dose (see Table S1). Note that PC's transmittance most likely decreased with increased UV irradiation time, but our instrument was incapable of measuring percent transmittances less than 0.1%.

**Table S1.** Polymer films' transmittance to 254 nm light with respect to UV exposure time.

Exposure Time (min)	%T <sub>254 nm</sub>		
	PMMA	COC	PC
0	1.2	53.8	0.1
2	1.1	56.5	0.1
5	0.8	53.0	0.1
10	0.6	43.5	0.1
15	0.5	36.8	0.1

**UV-induced polymer fragmentation and ablation assessed by TBO analysis.** TBO electrostatically binds to aliphatic or aromatic carboxylic acids due to their anionic charge when deprotonated at relatively high pH values (pH = 10.5).<sup>1,2</sup> Thus, surface carboxylic acid functional group densities can be calculated for the polymers investigated in this study using a TBO assay.

After incubating the UV-activated polymers with TBO, the substrates were thoroughly rinsed in the same buffer used for the TBO solution. Following washing, surface bound TBO molecules were released from the surface using a 40% acetic acid solution. After release of the surface-bound TBO, an aliquot of this solution was analyzed via UV-Vis spectroscopy to determine the concentration of TBO bound to the surface via the calibration curve shown in Figure S1. Using the concentration, volume, and surface area, we calculated the surface-confined functional group densities, and this value was corrected using surface roughness factors generated from atomic force microscopy (AFM) images of the same substrate (Figure S4). A small amount of nonspecific adsorption of TBO to the activated polymer surfaces was observed.<sup>3</sup>

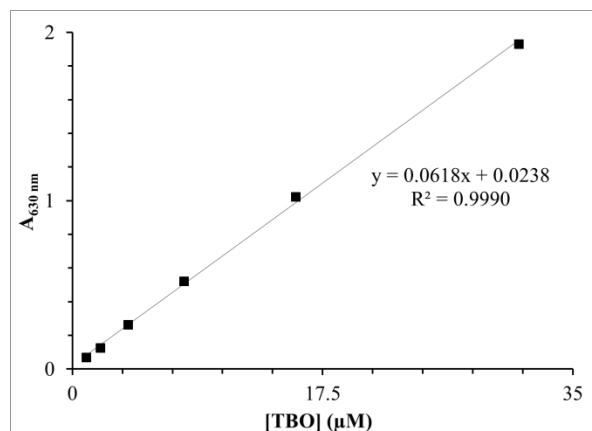


**Figure S1.** Calibration curve for TBO in 40% acetic acid measured at TBO's absorption maximum, which is 630 nm. For this calibration curve, known amounts of TBO were directly added to the buffer solution.

The 40% acetic acid solution was chosen to avoid dissolution of the PMMA surface, which occurred at >50% acetic acid concentrations. The 40% acetic acid solution could, however, potentially remove any photo-fragments generated by scissioning of the polymer backbone during UV irradiation and

thus produce low-molecular weight polymer chains (*i.e.*, photo-fragments).<sup>4,5</sup> We observed that 50% acetic acid solutions did produce noticeable dissolution of UV-activated PMMA surfaces. We concluded that the modified PMMA surface must differ in terms of its intermolecular forces compared to the unmodified material. This coincides with spectroscopic and water contact angle measurements suggesting the formation of oxidized species on the polymer's surface after UV exposure.

If we only incubated the surface with IPA and let the solvent evaporate, we visually observed an opaque residue deposit that was not observed for pristine PMMA (Figure S2). This residue was likely crystallization of PMMA photo-fragments. Furthermore, this residue's contact angle was  $95.4 \pm 15.8^\circ$ . This indicates that rearrangement of these fragments after solvent evaporation was similar to that generated during heating, where hydrophobic moieties are more prone to orient themselves towards the surface due to the interfacial air boundary, and perhaps shows that fragment rearrangement may also negatively impact functional group surface density. Note that the hydrophobicity indicated by this water contact angle is likely influenced by trapped air pockets within the high roughness of the opaque residue, which had an RMS roughness of 326.5 nm (Figure S2).<sup>6</sup>

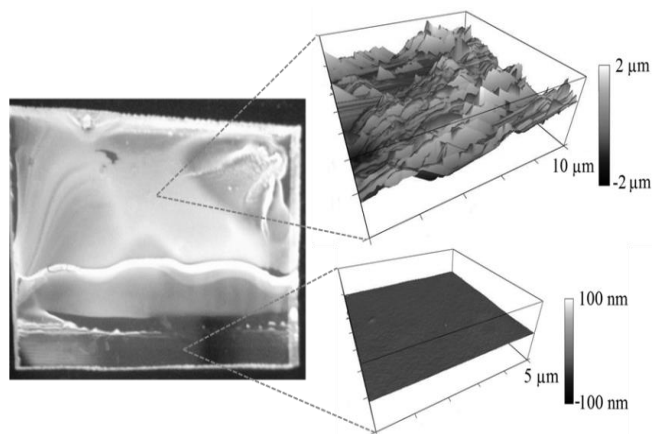


**Figure S2.** Opaque residue formed on a PMMA surface that was irradiated at 254 nm for 15 min (Power = 22 mW/cm<sup>2</sup>) after treatment with IPA and letting the solvent evaporate. AFM images were acquired on this residue and the clear surface.

Neither pristine nor UV-activated COC or PC exhibited the presence of this opaque residue as seen for PMMA (Figure S2). In the case of PC, photo-fragmentation is a minor process associated with UV treatment, and it is likely that crystallized fragments would be in too low quantity to be visually observable. This is also probably the case with UV-activated COC. The fact that TBO signals were significantly greater on UV-COC compared to UV-PMMA is likely a result of more efficient UV-induced carboxyl group formation on COC and less photo-fragmentation compared to PMMA (see main text).

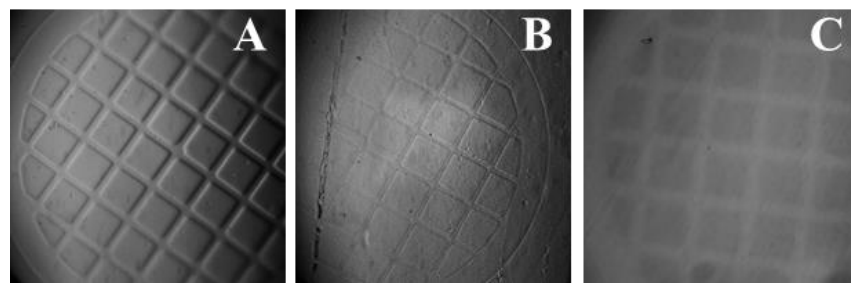


**Figure S3.** 10X optical images of (A) PMMA, (B) COC, and (C) PC substrates there were irradiated at 254 nm for 15 min (Power = 22 mW/cm<sup>2</sup>) through a Cu grid. Both (A) and (B) were taken in brightfield mode. Image (C) shows a fluorescence image taken with a FITC filter set of the PC substrate after UV-irradiation

showing autofluorescence for those areas exposed to UV radiation, but no contrast was seen for PC when acquired in brightfield mode.

To qualitatively assess photolytic ablation of the polymer substrates during UV-activation, we irradiated substrates through a fine copper grid that masked regions of the surface so that relative changes in UV-induced ablation could be determined with respect to unexposed regions. After modification, we secured brightfield images of these surfaces to observe the contrast between the irradiated and masked regions (Figure S3). No contrast was observed for the UV-treated PC surface, indicating very little photo-induced ablation. However, a fluorescence image of this surface showed significant increases in its autofluorescence in regions exposed to UV radiation.<sup>7</sup>

**AFM imaging.** AFM images were acquired to determine the surface morphology and RMS roughness for pristine, UV, and UV/thermal treatments of PMMA, COC, and PC substrates (Figure S4). RMS values and surface roughness correction factors were calculated, and these values were used to correct the functional group surface densities obtained from the TBO analyses.

Polymer	Modification		
	Pristine	UV	UV/thermal
PMMA	 RMS = 1.4 nm	 7.9 nm	 9.6 nm
COC	 4.8 nm	 18.5 nm	 12.0 nm
PC	 1.0 nm	 9.5 nm	 16.9 nm

**Figure S4.** AFM images and their corresponding RMS values for pristine, UV, and UV/thermal treated PMMA, COC, and PC substrates. All y-axes were scaled from values of -325 nm to 325 nm and all images were scanned over a surface area of 10  $\mu\text{m}$  by 10  $\mu\text{m}$ . The RMS value for pristine PC was calculated after removing 20  $\mu\text{m}^2$  of the surface area, which included the large object near the back of the image that was likely due to a small contamination. This decreased the RMS value from 31.8 nm to 1.0 nm, similar to that of the other pristine substrates.

**Water contact angles of several different PMMA substrates.** PMMA sheets have different manufacturing processes with various blends of additives to enhance the structural properties and to

prevent yellowing and/or degradation of the polymer by light exposure. For example, clinical-grade PMMA is produced with superior quality to ensure a higher and narrower molecular weight range. In addition, substrates acquired from the same manufacturer, but produced at different times, can compositionally differ as well.<sup>8</sup> The concern is that optimization of UV-activation procedures may have to be reassessed every time a new batch of PMMA is acquired. We briefly addressed this concern via water contact angle analysis as described in the main text.

We performed sessile water contact angle analysis on several types of PMMA. These substrates were obtained from different suppliers, numbers listed following the polymer name correspond to the numbering in Figure S5: Altuglas International (Bristol, PA) (1); Lucite International (Memphis, TN) (2); MacMaster (Aurora, OH) (3); Perspex (Umbogintwini, South Africa) (4); and two batches from Plaskolite Optics (Columbus, OH) (5,6). Also, we tested a clinical grade PMMA sample from Plaskolite Optics (7). Figure S5 compares the water contact angles over the course of UV-activation and thermal treatment, which was used to simulate thermal fusion bonding of a cover plate over the fluidic substrate.

For the pristine PMMA samples, water contact angles ranged from  $71.7 \pm 0.9^\circ$  to  $77.9 \pm 2.1^\circ$ . This variability could simply be due to differences in the substrates' thermal histories rather than due to differences in their chemical compositions. However, variations in the wettability of the substrates after UV modification were much larger, ranging from  $29.8 \pm 2.0^\circ$  to  $49.0 \pm 1.2^\circ$ . As mentioned, this could be due to different UV/radical scavengers present in the polymers and/or molecular weight distributions between different batches. Of interest was the return of all contact angles to nearly the same wettability after thermal treatment.

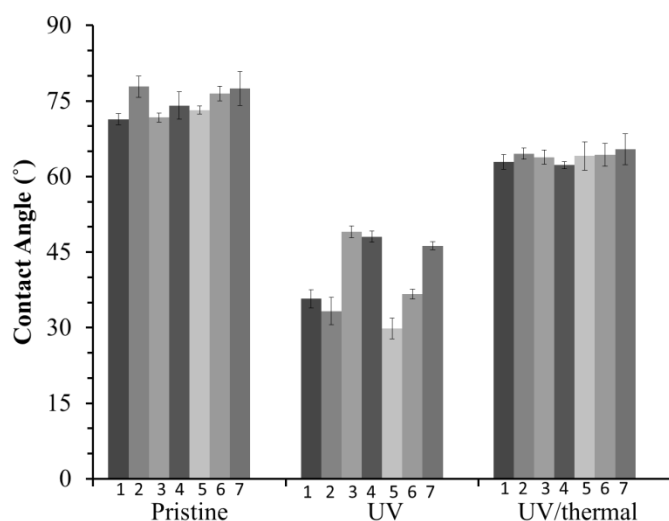


**Figure S5.** Water contact angles for seven PMMA samples from different suppliers, different batches and different grades. Refer to the text for numerical assignments of the samples and details of UV and UV/thermal treatments.

Return to the pristine wettability of the UV-activated material following thermal processing may be independent of chemical composition, additives, and/or molecular weight range of the polymer, but additional analyses must be performed to verify this. The hypotheses posed in the main text regarding

photo-fragment rearrangement could account for these observations. Thus, high doses of 254 nm radiation (22 mW/cm<sup>2</sup>, 15 min) may cause significant fragmentation of the PMMA polymer, and after heating, surface photo-fragments rearranged, generating nearly the same surface regardless of the initial material's composition.

Finally, using the Plaskolite sample 6, we observed that return to the pristine water contact angle was dependent on both annealing temperature and time. Heating the sample to 87°C for 20 min gave a contact angle of 59.6 ±0.8°; heating to 87°C for 30 min gave a water contact angle of 66.5 ±0.8°; and thermal treatment at 102°C for 20 min gave a water contact angle of 63.9 ±2.1°. Again, these results can be explained by thermal induced rearrangement of photo-fragments.<sup>9</sup>

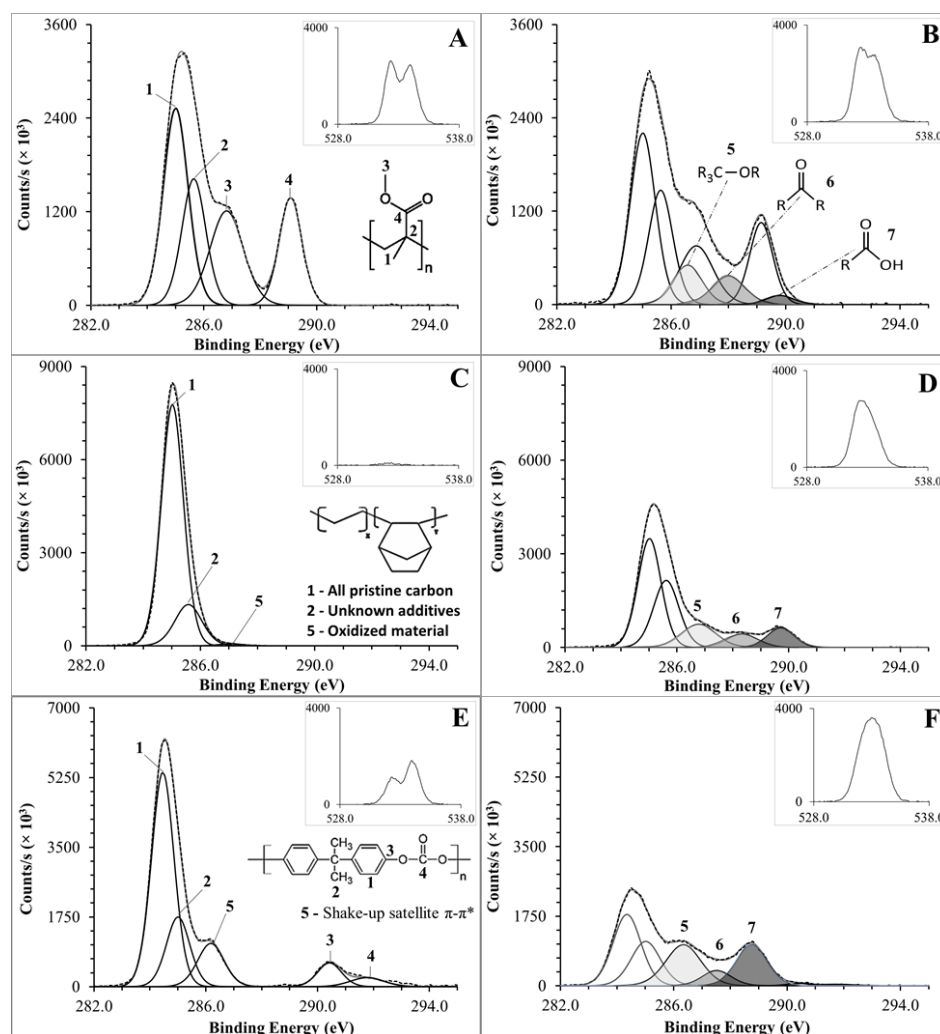
**Deconvolution of X-ray photoelectron spectra (XPS).** For all high resolution XPS spectra, a Shirley background was subtracted by averaging at least 10 end points that were associated with the background. Pristine C 1s spectra for PMMA, COC, and PC were deconvoluted based on previously published functional group binding energies.<sup>10-12</sup> After UV modification, peaks attributed to oxidized functionalities, namely alcohols/ethers, aldehydes/ketones, and carboxylic acids/esters, were added to the deconvolution method. As there were many sets of deconvoluted peaks, we logically deduced several realistic constraints to improve the accuracy of the resultant deconvoluted signals. As a matter of reference for the following description of the deconvolution methods, we present deconvoluted and labeled C 1s spectra for pristine and UV-activated substrates in Figure S6, and in Table S2, the accompanying deconvoluted C 1s atomic concentrations (as a percent of the total C 1s signal) and O 1s atomic concentrations (as a percent of total signal) are provided for all substrates and treatments.

Pristine PMMA's C 1s spectrum was deconvoluted into four Gaussian components: (1) 285.0 eV aliphatic C-C and C-H; (2) 285.6 eV quaternary C-C  $\alpha$  to the pristine ester; (3) 286.8 eV methoxy C-O ester; and (4) 289.1 eV carbonyl C=O ester. This fitting was in good agreement with previous literature, albeit the theoretical peak area ratio of the C 1s components (1) to (4) of 2:1:1:1 was found to be 2.00:1.00:1.29:1.24 in our data likely due to additives and plasticizers introduced by the manufacturer.<sup>13</sup>

The C 1s spectra of UV-activated PMMA contained three additional peaks accompanying the four pristine signals: (5) 286.6 eV alcohol and non-pristine ester C-O; (6) 288.0 eV aldehyde and ketone C=O; and (7) 289.8 eV carboxylic acid C=O. During the fitting of these additional peaks, we emplaced two primary constraints. First, each pristine peak's full width half maximum was maintained constant (this was applied to all deconvolution methods unless otherwise stated). Secondly, we recognized that if the pristine ester were photodegraded and generated additional functionalities, both the methoxy peak (3) and the carbonyl peak (4) would be equally affected. Therefore, the ratio of peak area between peaks (3) and (4) was maintained as close to 1.04 as possible, and the relative shift in binding energy was also

constrained to the pristine value, 2.3 eV. Besides widths, no constraints were emplaced on peaks (1) and (2) due to potential chemical crosslinking and fragmentation of the polymer backbone.<sup>4,14</sup>

The pristine COC C 1s spectrum was deconvoluted into three components: (1) 285.0 eV aliphatic C-C and C-H, which should comprise the entirety of carbon signals within pure COC; (2) 285.6 eV unknown carbon signals, likely due to additives; and (5) a small 287.0 eV C-O peak, which we attributed to a small amount of oxidized material.<sup>11</sup> After UV-activation, three peaks were added, C 1s components (5), (6), and (7), which have identical assignments as UV-activated PMMA. However, peak (7) is attributed entirely to carboxylic acids as esters are improbable photo-oxidation products for COC, which contains no alcohol or ether groups. Because the UV reaction pathway is unknown for COC, this is an assumption that could slightly skew the reported carboxyl group peak intensities. The widths of C 1s (1) and C 1s (2) peaks were not constrained after fitting the UV-activated material because the chemical environment of these atoms likely changed significantly after modification, but the widths of the UV/thermal peaks were constrained relative to the UV fitting data.





Pristine PC's C 1s spectrum was deconvoluted into the following peaks: (1) 284.5 eV aromatic C-C and C-H; (2) 285.0 eV aliphatic C-C and C-H; (3) 290.4 eV carbonate C=O; (4) 291.8  $\pi$ - $\pi^*$  shake-up satellite; and (5) 286.2 eV aromatic C-O. The ratio of peak areas of C 1s (1):(2):(3):(5) was 8.42:2.85:1.00:1.99, and matches reasonably well with the theoretical ratio of 10:3:1:2.

Modified PC spectra were deconvoluted by calibrating the C 1s (2) peak to 285.0 eV, fixing the C 1s (3) and C 1s (4) peaks at their pristine positions, adjusting the C 1s (1) peak within  $\pm 0.2$  eV of its pristine position, and adding C 1s (5), C 1s (6), and C 1s (7) peaks corresponding to phenols, alcohols, or ethers, aldehyde or ketone carbonyls, and ester or carboxylic acid carbonyls, respectively.

**Table S2.** Deconvoluted C 1s atomic concentrations (as percent of total C 1s signal), O 1s atomic concentration (as percent of total signal), and integrated FTIR absorbance peaks for the O-H and C=O absorption regions for all treatments of the PMMA, COC, and PC substrates. UV-activated substrates were irradiated at 254 nm for 15 min (Power = 22 mW/cm<sup>2</sup>).

Substrate	Treatment	C 1s Atomic Concentration (%)							O/C Ratio	FTIR Peak Area (au·cm <sup>-1</sup> )	
		(1)	(2)	(3)	(4)	(5)	(6)	(7)		O-H	C=O
PMMA	Pristine	36.2	18.1	23.3	22.4	-	-	-	0.32	3.1	21.4
	UV	36.2	17.3	15.2	14.6	5.9	8.9	2.0	0.38	13.9	25.2
	UV+102°C	38.9	20.1	16.4	15.7	1.7	6.0	1.2	0.32	8.5	24.8
COC	Pristine	78.1	22.0	-	-	-	-	-	0.01	0.0	0.0
	UV	43.5	28.6	-	-	11.4	7.6	8.9	0.27	13.4	11.2
	UV+130°C	62.7	22.9	-	-	6.4	4.7	3.4	0.10	7.8	10.5
PC	Pristine	56.9	19.3	3.6	6.8	13.5	-	-	0.15	1.3	18.1
	UV	30.4	19.8	0.4	1.2	21.8	6.7	19.5 <sup>1</sup>	0.48	7.6	18.6
	UV+145°C	37.7	19.8	0.8	1.2	19.0	6.6	14.9 <sup>1</sup>	0.40	5.7	19.3

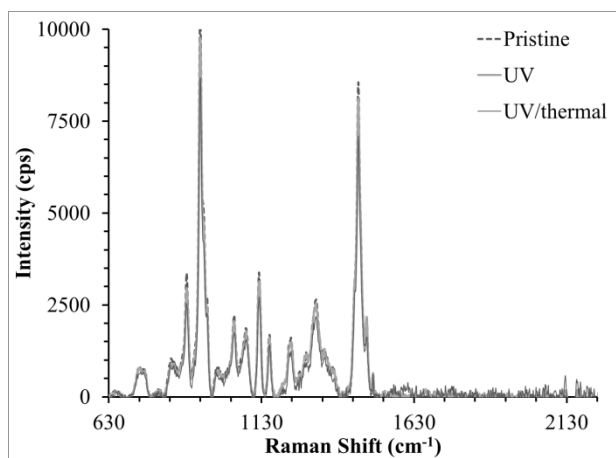


**Figure S7.** Background-subtracted Raman spectra of pristine, UV, and UV/thermal treated COC samples. The samples were irradiated at 254 nm for 15 min with a power density of 22 mW/cm<sup>2</sup>.

**Raman spectroscopy of COC substrates.** We acquired background subtracted Raman spectra for pristine COC, UV-treated COC and UV/thermally treated COC. We did not observe any new peaks over the course of the UV-activation process (Figure S7). Thus, the  $1637\text{ cm}^{-1}$  shoulder in UV-activated COC's FTIR spectra (Figure 3B) is not due to alkene formation but rather likely low energy stretching of aldehydes, ketones, or H-bonded carboxyls. Not shown in Figure S7 are differences in the uncorrected spectra's baselines. After UV treatment, a sloping baseline was observed that increased with the Raman shift. The intensity of this baseline increased further after thermal treatment. Due to the increase in signal at lower energies relative to the excitation wavelength, we attribute this to increases in autofluorescence of the COC substrate after UV and UV/thermal treatment.

**Analyses of UV-activated and thermally treated PC substrates.** Within the context of our results showing that functionalized photo-fragments bury into the bulk polymer upon thermal treatment and become inaccessible, PC serves as an excellent comparison to PMMA and COC as PC tends to resist ablation and scissioning due to the well-known photo-Fries rearrangement.<sup>15</sup> For instance, no ablation of the PC surface was apparent after UV-activation via contrast in brightfield microscopy, only an increase in autofluorescence was apparent (Figure S3C).<sup>7</sup> Therefore, we expect that the thermal effects observed for PMMA and COC should be less pronounced for PC.

PC's native water contact angle was  $87.0 \pm 2.0^\circ$ , which reduced to  $17.3 \pm 1.0^\circ$  after UV exposure. Correspondingly, the pristine-subtracted TBO results produced a functional group density of  $4.0 \pm 0.6\text{ nmol/cm}^2$ . This value is again greater than physically possible for a monolayer<sup>16</sup> (see main text) and indicates some fragmentation on the UV-activated PC surface, albeit to a much less extent than that observed for PMMA and COC. For instance, there is clear degradation of the UV-PC surface in the AFM image shown in Figure S4. However, the TBO analysis was fundamentally complicated by the photo-Fries rearrangement products, which included phenols that can be deprotonated at the carbonate buffer's pH (10.5). Therefore, for TBO analysis of PC, we cannot discern the presence of carboxy products, which are generated via competitive side-chain oxidation<sup>10</sup>, from the phenol photo-Fries products.

To identify the photo-products on the UV-PC surface, we employed both XPS and ATR-FTIR spectroscopies. After UV-activation, a 0.33-fold increase in the O/C ratio was observed due to the appearance of several oxidized carbon species (Figure S6E, F), which were deconvoluted in Table S2 according to the protocol outlined above. Note that we could not logically deduce an accurate method to deconvolute ester signals, such as in the phenylsalicylate photo-Fries rearrangement product (Figure S8), from carboxyl signals. Together, these signals comprised 19.6% of the C 1s signal after UV-activation.

ATR-FTIR peak areas indicated the presence of several new oxidized functionalities, such as an increase of  $0.5\text{ au}\cdot\text{cm}^{-1}$  and  $6.3\text{ au}\cdot\text{cm}^{-1}$  for the C=O ( $1650\text{-}1850\text{ cm}^{-1}$ ) and O-H ( $3200\text{-}3700$ ) regions,

respectively (Table S2). More specifically, using the work of Rivaton, *et al.*, we were able to identify several photo-products from the pristine-subtracted carbonyl region of PC's ATR-FTIR spectra (Figure S9).<sup>10</sup> These products are shown in Figure S8 along with their corresponding carbonyl stretching energies, which are matched to the pristine-subtracted UV PC and UV/thermal PC spectra as shown in Figure S9.

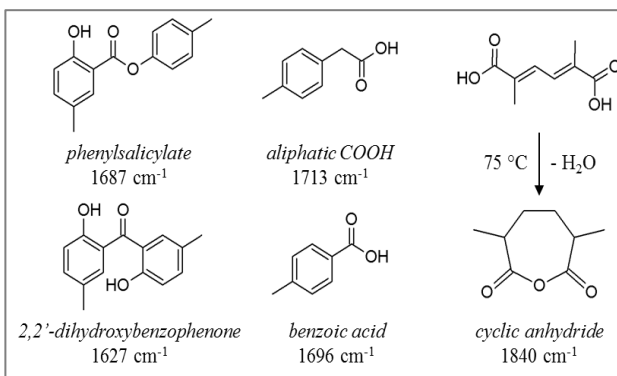


**Figure S8.** Structures and carbonyl stretching frequencies of PC's photo-Fries rearrangement and photo-oxidation products.<sup>10</sup>

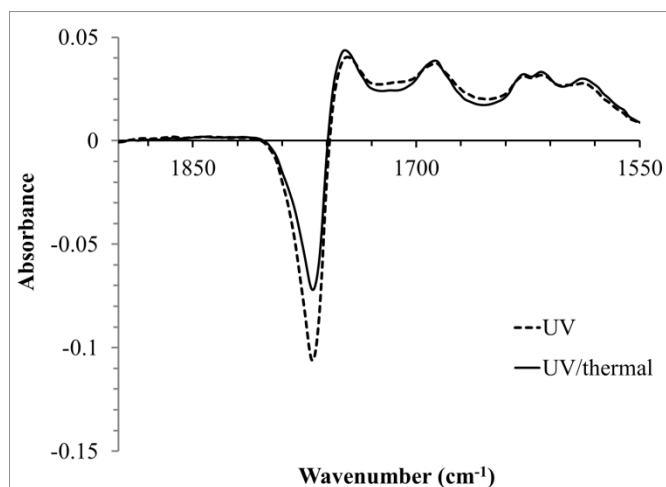


**Figure S9.** Carbonyl regions of the pristine background subtracted FTIR spectra for PC substrates that were UV-activated (UV) and subsequently thermally treated (UV/thermal) at 145°C for 20 min.

Despite being convoluted, we were able to identify several peaks in addition to the pristine carbonate stretch (1767 cm<sup>-1</sup>) that were generated by UV-activation. The photo-Fries rearrangement products, 2,2'-dihydroxybenzophenone (1627 cm<sup>-1</sup>) and phenylsalicylate (1687 cm<sup>-1</sup>), were apparent along with their associated O-H ring substitutions (1617 and 1585 cm<sup>-1</sup>) and H-bonded carbonate groups (1748 cm<sup>-1</sup>).<sup>10</sup> The constant level of atomic oxygen and ozone in the modification chamber (see main text) may have also led to photo-oxidation of the gem dimethyl side chains, producing aliphatic carboxylic acids (1713 cm<sup>-1</sup>) and benzoic acids (1696 cm<sup>-1</sup>). There was also a very small peak at 1840 cm<sup>-1</sup>, which could have originated from ring scissions producing aliphatic carboxylic acids that can rearrange to form cyclic anhydrides at the elevated temperatures present in our system. Rivaton, *et al.* observed this rearrangement from 45°C to 75°C, and these conditions occurred within the modification chamber,

which was heated to 50°C after a 15 min UV exposure time.<sup>10</sup> However, this peak is small enough that it could be an artifact of background subtraction.

After thermally treating UV-PC, the surface retained enhanced wettability compared to the native material with a water contact angle of  $50.9 \pm 0.5^\circ$ ; degradation of the surface's morphology was still evident in AFM images (Figure S4); the TBO signal decreased by  $30 \pm 9\%$ ; the O/C ratio and COOH/ester C 1s signals decreased by 17% and 24.0%, respectively; the O-H ATR-FTIR peak area decreased by 30%, and the C=O ATR-FTIR peak area increased by 140% due to reemergence of the pristine signal and potentially reordering of the surface (Table S2). It is also interesting to note when analyzing the ATR-FTIR C=O region (Figure S9), nearly all photo-products' signals decreased except for the peaks attributed to the primary photo-Fries products, 2,2'-dihydroxybenzophenone and phenylsalicylate. These trends qualitatively match that of PMMA and COC, most likely due to some photo-fragmentation, but in terms of magnitude, thermal effects were less significant because clear signs of oxidative species remained.

Fluorescence imaging of Cy3-labelled oligonucleotide reporters was complicated by PC's considerable autofluorescence post-modification (Figure S3).<sup>7</sup> The background-subtracted fluorescence signal of Cy3-labelled oligonucleotides covalently coupled to carboxy groups on planar, UV and UV/thermal PC was  $296 \pm 169$  cps and  $282 \pm 168$  cps, respectively. The carboxy content on the UV-PC surface was relatively unaffected by thermal treatment, which supports the hypothesis that the resistance of a modified surface to thermal migration of hydrophilic functional groups away from the surface is intimately tied with its tendency to scission upon modification.

PC microchannel modification showed little correlation with aspect ratio, retaining  $82 \pm 6\%$  and  $72 \pm 33\%$  TBO signal (relative to a planar surface) at aspect ratios of 1.25 and 2.00, respectively. Considering the poor transmissivity of the polymer, this was unexpected and may be due to PC's propensity for undergoing the photo-Fries rearrangement even at low fluxes of UV radiation.<sup>10</sup> Because we are incapable of distinguishing phenols from carboxyls on modified PC surfaces using TBO analyses and were unable to acquire fluorescence data within microstructures, this interpretation is far from certain. Finally, the PC polymer was disqualified from CTC analysis because we would be unable to image and identify fluorescently-labeled cells due to its large autofluorescence background.<sup>7</sup>

**Fluid Dynamics Simulations through Curvilinear Channel Architectures.** To investigate the dynamics of fluid flow through the curvilinear microchannels, we conducted CFD simulations using COMSOL Multiphysics® 4.3a. The hot-embossed curvilinear channel architectures was constructed in three dimensions using AutoCAD and SolidWorks and imported into COMSOL, where a mapped mesh was applied to the cross section and swept across the curvilinear channel to generate a final mesh with >1,600,000 elements (shown with dimensions in Figure S10).

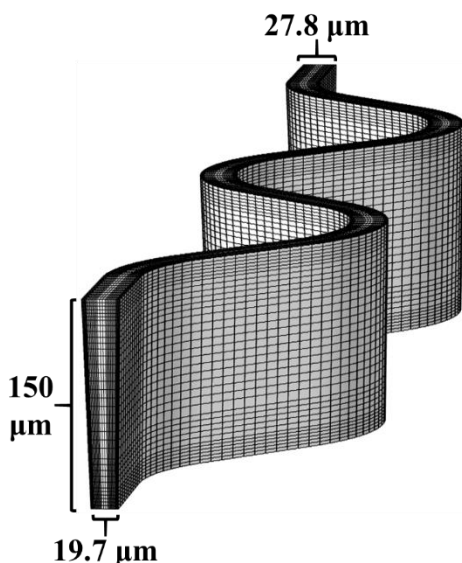


**Figure S10.** Meshed geometries for CFD simulations of curvilinear channels with trapezoidal cross sections after hot-embossing and stringent annealing (see main text). Each mesh contains >1,600,000 elements (shown on the geometries' surfaces as a black grid).

Laminar flow was applied throughout the geometry with inlets and outlets for the fluid governed by the experimental linear velocity for optimal CTC capture (see main text) and solved using the PARDISO algorithm, pseudo-time stepping, and a minimum convergence tolerance of at least  $10^{-4}$ . In the case of describing blood's non-Newtonian behavior, the Carreau model was applied, where the effective viscosity ( $\mu_{eff}$ ) was given by;

$$\mu_{eff} = \mu_{\infty} + (\mu_0 - \mu_{\infty})[1 + (\lambda \cdot \dot{\gamma})^2]^{\frac{n-1}{2}}, \quad (S2)$$

where  $\mu_{\infty} = 0.0345 \text{ g}/(\text{cm} \cdot \text{s})$  and  $\mu_0 = 0.56 \text{ g}/(\text{cm} \cdot \text{s})$  and are blood's viscosity at infinite and zero shear rate ( $\dot{\gamma}$ ), respectively,  $\lambda = 3.313 \text{ s}$  is the relaxation time, and  $n = 0.3568$  is the power index. Additionally, the blood's density ( $\rho$ ) was set to  $1.06 \text{ g}/\text{cm}^3$ .<sup>17,18</sup>

## References

1. Y. Wang, M. Bachman, C. E. Sims, G. P. Li and N. L. Allbritton, *Langmuir : the ACS journal of surfaces and colloids*, 2006, **22**, 2719-2725.
2. E. Uchida, Y. Uyama and Y. Ikada, *Langmuir : the ACS journal of surfaces and colloids*, 1993, **9**, 1121-1124.
3. A. Tiraferri and M. Elimelech, *Journal of Membrane Science*, 2012, **389**, 499-508.
4. S. Wei, B. Vaidya, A. B. Patel, S. A. Soper and R. L. McCarley, *The journal of physical chemistry. B*, 2005, **109**, 16988-16996.
5. C. Wochnowski, M. A. Shams Eldin and S. Metev, *Polym Degrad Stabil*, 2005, **89**, 252-264.
6. D. Quéré, *Physica A*, 2002, **313**, 32-46.
7. H. Shadpour, H. Musyimi, J. F. Chen and S. A. Soper, *Journal of Chromatography A*, 2006, **1111**, 238-251.
8. C. P. MacDermott and A. V. Shenoy, *Selecting thermoplastics for engineering applications*, M. Dekker, New York, 1997.
9. G. S. Y. Yeh, R. Hosemann, J. Loboda-Čačković and H. Čačković, *Polymer*, 1976, **17**, 309-318.
10. A. Rivaton, *Polym Degrad Stabil*, 1995, **49**, 163-179.
11. S. Roy, C. Y. Yue, Y. C. Lam, Z. Y. Wang and H. Hu, *Sensors and Actuators B: Chemical*, 2010, **150**, 537-549.
12. C. Seidel, H. Kopf, B. Gotsmann, T. Vieth, H. Fuchs and K. Reihls, *Applied Surface Science*, 1999, **150**, 19-33.
13. S. Ben Amor, G. Baud, M. Jacquet, G. Nansé, P. Fioux and M. Nardin, *Applied Surface Science*, 2000, **153**, 172-183.
14. This width constraint may produce slight error since these reactions could change the chemical environment of the atoms generating these signals. However, any error generated by this

constraint would not likely impact the fitting of oxidized species, especially carboxy fitting, and so this was accepted as a necessary restriction.

15. A. Rivaton, D. Sallet and J. Lemaire, *Polymer Degradation and Stability*, 1986, **14**, 23-40.
16. A monolayer of TBO molecules with this density implies each TBO molecule occupies  $4.0 \text{ \AA}^2$ , which is physically impossible.
17. S. Amornsamankul, B. Wiwatanapataphee, Y. H. Wu and Y. Lenbury, *Int. J. Biol. Life Sci.*, 2005, **1**, 42-46.
18. A. Razavi, E. Shirani and M. R. Sadeghi, *J Biomech*, 2011, **44**, 2021-2030.